OPEN

Biaxial Compressive Strain Engineering in Graphene/Boron Nitride Heterostructures

Wei Pan[1], Jianliang Xiao[2], Junwei Zhu[1], Chenxi Yu[3], Gang Zhang[3], Zhenhua Ni[4], K. Watanabe[5], T. Taniguchi[5], Yi Shi[1] & Xinran Wang[1]

[1]National Laboratory of Microstructures, School of Electronic Science and Engineering, Nanjing University, Nanjing 210093, China, [2]Department of Mechanical Engineering, University of Colorado, Boulder, CO 80309-0427, USA, [3]Key Laboratory for the Physics and Chemistry of Nanodevices and Department of Electronics, Peking University, Beijing 10087, China, [4]Department of Physics, Southeast University, Nanjing 211189, China, [5]Advanced Materials Laboratory, National Institute for Materials Science, 1-1 Namiki, Tsukuba, 305-0044, Japan.

Strain engineered graphene has been predicted to show many interesting physics and device applications. Here we study biaxial compressive strain in graphene/hexagonal boron nitride heterostructures after thermal cycling to high temperatures likely due to their thermal expansion coefficient mismatch. The appearance of sub-micron self-supporting bubbles indicates that the strain is spatially inhomogeneous. Finite element modeling suggests that the strain is concentrated on the edges with regular nano-scale wrinkles, which could be a playground for strain engineering in graphene. Raman spectroscopy and mapping is employed to quantitatively probe the magnitude and distribution of strain. From the temperature-dependent shifts of Raman G and 2D peaks, we estimate the TEC of graphene from room temperature to above 1000K for the first time.

Graphene has attracted wide attention for both fundamental physics and potential application in electronics[1–3]. Recently, hexagonal boron nitride (h-BN, abbreviated as BN in the following) has been proposed as an ideal substrate[4–8] and tunnel barrier[9] for graphene devices because it is atomically flat with little dangling bonds and charge traps. Devices based on graphene/BN (GBN) heterostructures have shown much higher mobility, less intrinsic doping[4–8] and improved on/off ratio[9] than conventional devices structures on SiO$_2$ substrate. On the other hand, because of the reduced interaction with substrate, GBN is also an appealing system to study intrinsic mechanical properties of graphene which has been rarely explored in GBN thus far. In particular, strain has been shown to effectively tailor the electronic properties of graphene for all-graphene electronics, pseudomagnetic field, and tunable bandgaps[10–16]. Recently, it is proposed that exploiting the different thermal expansion coefficient (TEC) between graphene and substrate could realize the desirable strain distribution for electronic device applications[13,17]. Experimentally, Bao et al. formed 1D ripple textures in suspended graphene[17], while Yoon et al. achieved a uniform compressive strain ~0.05% in graphene on SiO$_2$ by thermal cycling[18]. However, the strain distribution in these systems were not well understood, which hinders the rational design of strain-based electronic devices.

Results

In this work, we utilize the different TEC of graphene and BN to engineer the strain in GBN heterostructures. After thermal cycling, large amount of triangular and polygonal graphene bubbles appear partly due to mechanical buckling under biaxial compressive strain. Finite element mechanical simulations show good agreement with experiments and reveal the strain distribution in the bubbles, which is further supported by Raman mapping. The spatially inhomogeneous strain distribution in graphene may be interesting for electronic device applications[10–14]. Finally, we use Raman spectroscopy to quantitatively measure the temperature-dependent compressive strain in GBN due to TEC mismatch and derive the TEC of graphene over a wide temperature range.

Atomic force microscopy characterizations of GBN samples. Single-layer GBN structures were made by a commonly used mechanical transfer technique[4,7,8] (Fig. 1a, S1, the experimental details are described in Supplementary Information). We annealed the GBN in Ar atmosphere and employed atomic force microscopy (AFM)
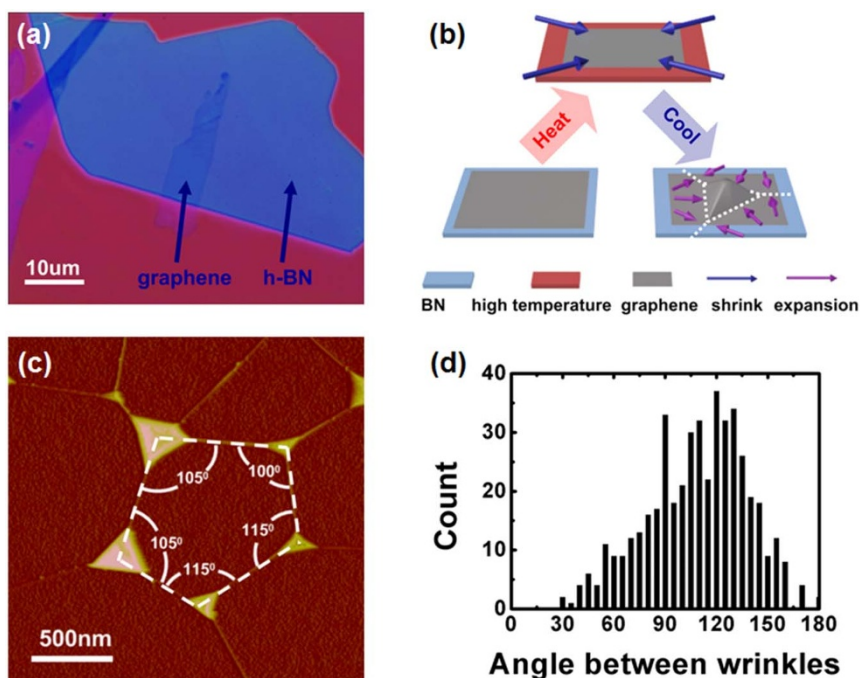
Figure 1 | (a) Optical image of a single-layer GBN sample on 300nm SiO$_2$. (b) Schematics of the proposed formation process of graphene bubbles and ridges on BN. (c) A representative AFM image of GBN bubbles and ridges after thermal annealing. Angles between the adjacent ridges are indicated. (d) Distribution of the angles between neighboring ridges showing a peak around 120 degree.
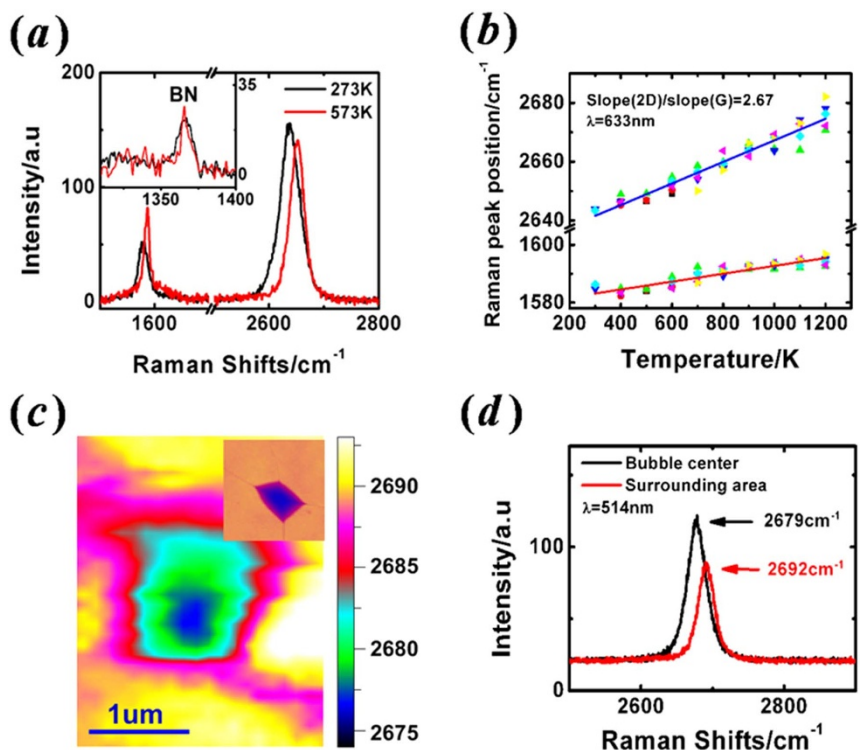

Figure 2 | (a) Raman spectra of the same GBN before and after 300C annealing. The inset compares the Raman peak of BN before and after annealing. The shifts in G and 2D peaks are not caused by system error as the BN peaks line up nicely for the two scans. We also carefully calibrated the spectrometer for each measurement. (b) Averaged G and 2D peaks positions of seven GBN samples as a function of annealing temperature. Solid lines are linear fittings of the data. The ratio between the linear temperature coefficient of 2D and G peak is 2.67. (c) A Raman mapping of 2D peak position near a graphene bubble with a 514 nm laser excitation. The bubble forms after annealing at 100°C. Inset shows the AFM of the bubble, sharing the same scale bar with (c). (d) The averaged Raman spectra taken at the bubble center and surrounding area from (c).

to characterize the samples. After annealing, we observed a large number of graphene bubbles,[5] typically covering ≲~5% of the total area (Fig. 1c). The bubbles were interconnected by 1D ridges to form many 2D domains in the GBN. Statistical study showed that the average size and height of the bubbles were ~300 nm and ~23 nm respectively (Fig. S2), much larger than graphene bubbles observed on metal surface[16,19]. As a result, typical triangular bubbles in GBN introduced a much smaller pseudo-magnetic field on the order of 1T (Ref. 16). The angle distribution between the neighboring ridges peaked at 120 degree (Fig. 1d), which is likely due to the symmetric nature of the interaction between the hexagonal graphene and BN lattices. Previous studies have demonstrated that van der Waals interaction between two parallel hexagonal lattices shows triangular symmetry, with three energy minima forming 120 degree angles[20,21].

Raman spectroscopic study of GBN samples. Raman spectroscopy is a powerful tool to investigate the mechanical and thermal properties of graphene[22]. For the as-made single layer GBN samples, three characteristic peaks appeared in the Raman spectrum ranging from 1300 cm^{-1} to 2900 cm^{-1}, namely BN peak (~1366 cm^{-1}), graphene G peak (~1580 cm^{-1}) and 2D peak (~2640 cm^{-1}), without any defect-related peaks (Fig. 2a). We then gradually increased the annealing temperature of the GBN samples from 100°C to 900°C and did Raman mapping after each thermal cycling. Fig. 2a shows the typical Raman spectra of the same GBN as-made and after annealing at 300°C, with clear blue shifts of G and 2D peaks after annealing. Such measurements were repeated on seven samples (Fig. 2b). In order to minimize the effect of inhomogeneous strain distribution within the GBN[7], each data point in Fig. 2b represented the average G or 2D peak position from a Raman mapping (typically a few hundred curves). We observed a linear temperature evolution of the peak positions, with different slopes for G and 2D peaks.

Two possible explanations for the peak evolution are compressive strain and charge doping[22–26]. However, we rule out the possibility of charge doping because 2D peak shift is less sensitive to doping than G peak[22,25], which contradicts our data. In addition, BN has been shown to introduce negligible charge doping to graphene[4–8], which is not likely to shift the 2D peak by ~30 cm^{-1} (Fig. 2b, Ref. 25). On the other hand, under biaxial strain ε^{biax}, Raman peaks shift linearly as

$$\Delta\omega_{G(2D)} = -2\gamma^{biax}_{G(2D)}\omega^0_{G(2D)}\varepsilon^{biax}, \qquad (1)$$

where γ^{biax} is the Grüneisen parameter and ω^0 is the unstrained peak position[22]. In the literature, the reported values of $\gamma^{biax}_{G(2D)}$ show variations up to ~40%[22]. We adopted the values from *ab-initio* calculations in Ref. 27 ($\gamma^{biax}_G = 1.8$, $\gamma^{biax}_{2D} = 2.7$) for quantitative analysis because they agreed well with experiments[28] and other calculations[29]. We fit the peak evolution in Fig. 2b with linear function and obtained the linear coefficient

$$\frac{\partial\omega_{G(2D)}}{\partial T} = -2\gamma^{biax}_{G(2D)}\omega^0_{G(2D)}\frac{\partial\varepsilon^{biax}}{\partial T} = \beta_{G(2D)}\frac{\partial\varepsilon^{biax}}{\partial T} \qquad (2)$$

to be 0.0138 cm^{-1}/K and 0.0369 cm^{-1}/K for G and 2D peaks respectively. The ratio between the slopes ($\frac{0.0369}{0.0138} \approx 2.67$) is in excellent agreement with the expected ratio of the pre-factors due to compressive strain $\frac{\beta_{2D}}{\beta_G} = \frac{\gamma^{biax}_{2D}\omega^0_{2D}}{\gamma^{biax}_G\omega^0_G} \approx 2.7$. Therefore, we attributed the Raman peak evolution to compressive strain in the GBN after thermal cycling[22]. As expected, the strain was biaxial in nature as we did not observe any peak splitting over the entire temperature range[23].

Strain engineering is an effective way to tailor the electrical properties of graphene. Yet many interesting phenomena require carefully designed strain distribution in graphene[10–16]. The presence of

bubbles introduces strain inhomogeneity that may enable unique strain-engineered devices based on GBN. To probe the strain distribution in GBN, we did Raman mapping on individual graphene bubbles (see Supplementary Information for details). Fig. 2c is the mapping of 2D peak position near the bubble shown in the inset. The bubble is clearly resolved together with the individual ridges extending from the corners (Fig. 2c inset). The 2D peak in the center is red-shifted by ~13 cm^{-1} (therefore less compressively strained) compared to the surrounding area (Fig. 2d), which corresponds to $\Delta\varepsilon^{biax} = \frac{\Delta\omega_{2D}}{2\gamma^{biax}_{2D}\omega^0_{2D}} \approx 0.09\%$. However, $\Delta\varepsilon^{biax}$ is underestimated due to averaging effects since the size of the bubble (~400 nm × 300 nm) is much smaller than the laser spot size (~1 um). After considering the area fraction of the bubbles to the laser spot size, the effective $\Delta\varepsilon^{biax}$ is ~0.6%, consistent with our finite element modeling discussed below.

Finite element mechanical modeling of graphene bubbles. To understand the bubble formation and quantitatively capture the strain distribution in graphene bubbles, we conducted finite element simulations for typical bubbles observed in experiment (Fig. 3a–f). We approximated the experimental data to structures with high symmetry to capture the essential mechanics. The details of the finite element simulations are described in Supplementary Information). The bubbles exhibit great diversity in size, shape and topolography. The bubble in Fig. 3e (experimentally in Fig. 1c and 3b) was relatively flat or even slightly volcano-shaped with the center lower than the surroundings, because of the combined effect of multiple edge wrinkles. This is different from the bubble in Fig. 3d (experimentally in Fig. 3a), due to their different geometrical aspect ratios. The simulated out-of-plane displacements (Fig. 3d–f) closely resembled the deformation patterns and heights of experimental results (Fig. 3a–c). The edges in the simulated structures exhibited nano-scale wrinkle structures due to the extreme flexibility of mono-layer graphene, although they were not clearly observed in experiments possibly due to limited lateral resolution of AFM. The strain distribution in the bubbles (Fig. 3g–i) is relatively uniform with magnitude close to zero, as the formation of bubbles release most of the compressive strains via nonlinear buckling mechanics. However, the strain is concentrated near the edges, because of the constrained strain release and wrinkle formation at the edges[30]. Such strain distribution is consistent with our Raman mapping (Fig. 2c). The local strain at the edges is ~0.6%–1% for the simulated structures. The locally strained edges are similar to the structures studied in recent theoretical papers[12,31]. Although the strain is still too small to open bandgap for realistic devices[12], it can be further increased by decreasing bubble sizes (Fig. S3). In addition, the bubbles in GBN are much larger than those observed on metal surfaces[16,19], therefore making electrical contacts to individual bubbles is possible.

Discussion

Bubbles were observed previously in GBN[5,7,32], but the origin was still under debate. Possible explanation included trapped hydrocarbons[7,39], gas bubbles[28,36] and pre-existing strain in graphene[32]. Recently, Haigh et al. brought direct evidence of hydrocarbons under graphene bubbles[39]. Although we cannot rule out the possibility of hydrocarbons in our case, our Raman and finite element modeling suggest the biaxial compressive strain in graphene is also important in the formation of the bubbles (the detailed discussion of possible bubble formation mechanism is in supplementary information). Fig. 1b describes the possible formation process of the bubbles. Because of the weak interaction between graphene and BN, during heat-up, the graphene contracted and slided relative to the BN substrate due to TEC mismatch. During cool-down, the graphene expanded and experienced a biaxial compressive stress[17,18]. The bending stiffness of graphene (~1.4 eV)[33] is so small that slight
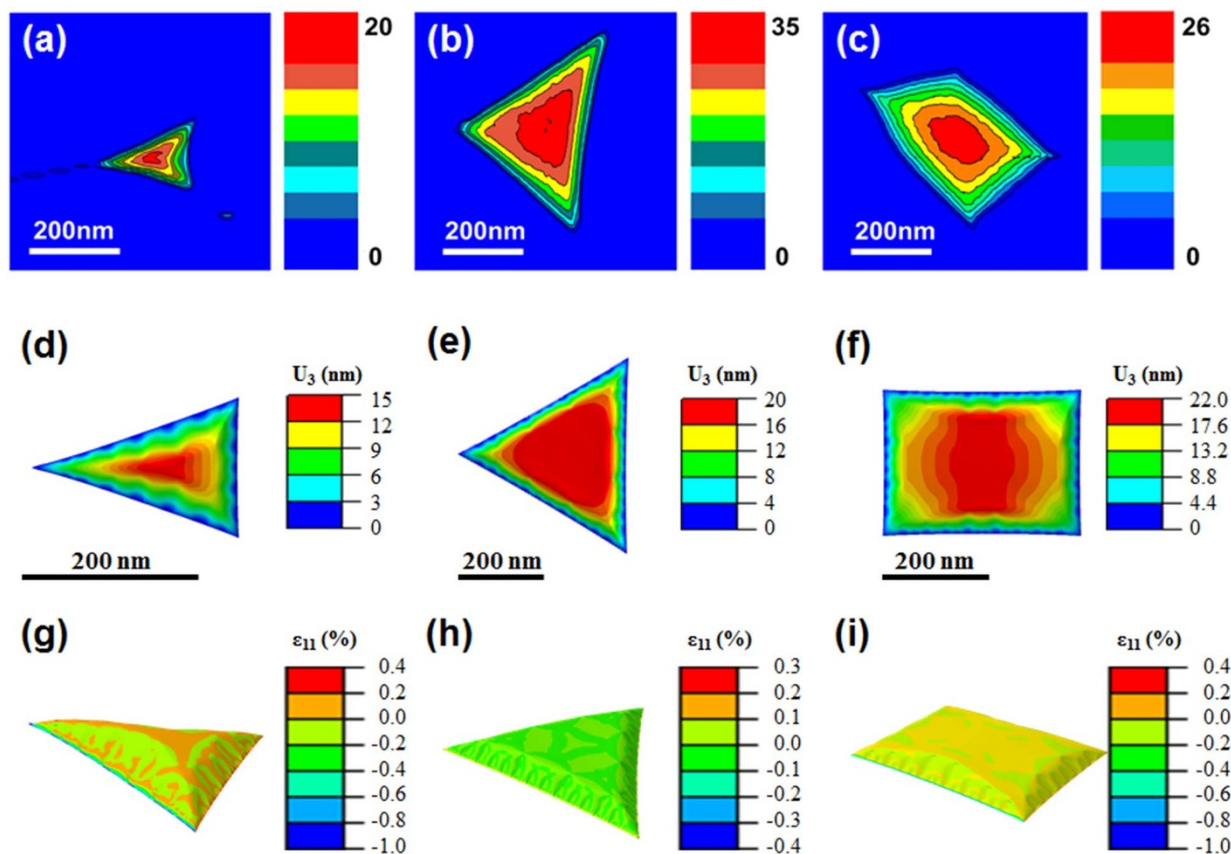
3

Figure 3 | (a), (b) and (c) AFM height images of three representative bubbles with triangular and quadrilateral shapes respectively. (d), (e) and (f) The simulated out-of-plane displacements of the three bubbles shown in (a)–(c) respectively. (g), (h) and (i) Strain (ε_{11}, the normal strain along horizontal direction) of the simulated bubbles shown in (d)–(f).

compressive stress can cause graphene to buckle and delaminate away from the substrate at weak interfacial interaction locations, forming nano-scale bubbles and ridges. For such buckling mechanism under a constant strain, linear correlation between the height and size of the bubbles (Fig. S2c) is expected. We also carried out *in situ* AFM at elevated temperatures to study the bubbles at different temperatures. Fig. S5 shows the AFM of the same area during 50°C and 100°C annealing in ambient respectively. Many bubbles became smaller or even disappeared at higher temperatures, presumably due to contraction of graphene relative to BN. We note that the bubbles observed here are distinct from those owing to trapped gas on SiO$_2$ substrate[28,36,37], where the round-shaped bubbles form without any thermal treatment and experience tensile strain. It is well known that BN has a negative in-plane TEC from room temperature to 770°C[34]. Therefore, the appearance of the bubbles indicates that graphene also has a negative TEC over a broad temperature range[29,35], which is confirmed by molecular dynamics (MD) simulation (Fig. S4a, the details are in Supplementary Information).

The strain induced by TEC mismatch $\Delta\varepsilon^{TEC}(T) = \dfrac{\Delta\omega_{G(2D)}}{2\gamma_{G(2D)}\omega^0_{G(2D)}}$ could be estimated from Fig. 2b, where $\Delta\omega_{G(2D)}$ is the Raman peak shift relative to the room temperature value. This can minimize the effect of pre-existing strain in graphene[32]. In Fig. 4a, we plot the temperature-dependent $\Delta\varepsilon^{TEC}$ derived from 2D peak evolution in Fig. 2b (G peak evolution gave similar results). In the case of small strain,

$$\Delta\varepsilon^{TEC}(T) = \int_{RT}^{T} [\alpha_G(T) - \alpha_{BN}(T)]dT \tag{3}$$

The linear temperature dependence of $\Delta\varepsilon^{TEC}(T)$ up to 900°C (Fig. 4a) suggested a constant difference in the TEC of graphene

and BN throughout the studied temperature range. Using the well-documented value of $\alpha_{BN}(T)$ by X-ray diffraction (up to ~800°C)[34], we can numerically derive that

$$\alpha_G(T) \approx -6.6 \times 10^{-6} + 3.8 \times 10^{-9}T \tag{4}$$

as plotted in Fig. 4b. We note that Eq. (3) has two hidden assumptions. First, at the highest temperature of each thermal cycling, graphene is unstrained, which is valid if graphene were completely decoupled from the substrate. Second, the strain is not released during cool down. However, the finite (although small) interaction of graphene and BN and partial release of strain makes the derived TEC a lower bound. Even then, $\alpha_G \approx -5.5 \times 10^{-6}/K$ at room temperature, well within the range of experimental values measured from suspended and supported graphene[17,18], which suggest that Eq. (3) is still qualitatively valid in our analysis. However, the earlier experiments were unable to measure the TEC of graphene beyond ~400K. Our derived $\alpha_G(T)$ shows a much weaker temperature dependence than the previous experimental results[17,18] and agrees well with the first-principle calculations by Mounet et al. over a wide temperature range[29]. In addition, we did MD simulations with Tersoff empirical bond order potential[38] to calculate the bond length of graphene up to 600K. The calculated bond length agrees well with both the first-principle calculations[29] and Eq. 4 (Fig. S4b). Possible sources of error in our analysis are discussed in the Supplementary Information.

In summary, we combined AFM, Raman spectroscopy and mapping, and mechanical modeling to study the biaxial compressive strain formation and distribution in GBN samples. Nano-scale bubbles appear partially as a result of mechanical buckling, creating interesting strain engineered graphene structures. Based on the strain evolution in GBN, we obtain the TEC of graphene over a wide
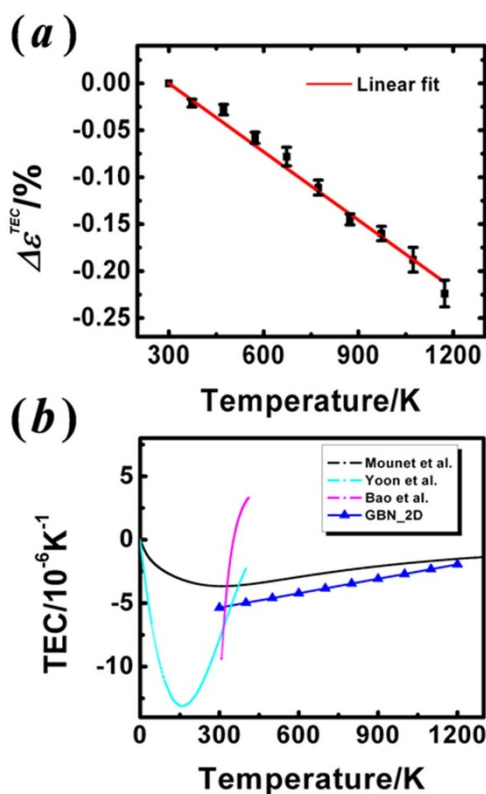
Figure 4 | (a) $\Delta\varepsilon^{TEC}$ as a function of temperature derived from the 2D peak shifts in Fig. 2b. The red line shows linear fitting. (b) The temperature-dependent TEC of graphene derived from $\Delta\varepsilon^{TEC}$, together with earlier theoretical and experimental results. The blue symbols are obtained from 2D peak shift in the present work (G peak shift gives similar results). The black line denotes the first-principle simulation results in Ref. 29. The purple and light blue lines denote the fitting of experimental values reported in Ref. 17 and 18 respectively.

temperature range, which agrees well with first-principle and MD calculations.

Methods

Fabrication and AFM characterization of GBN. We exfoliated single crystal BN flakes (~10 nm thick, ~100 μm in size) and single-layer graphene (Grade 300 Kish graphite, Graphene Laboratories, Inc.) onto separate 300 nm SiO2/Si substrates (Fig. S1a and S1b). The BN samples were annealed at 700°C in 5% H_2 in Ar atmosphere to remove possible organic contaminants. Optical microscope, Raman spectroscopy and AFM were used to confirm single-layer nature of graphene. After a brief baking step at 80°C, PMMA was spin coated onto graphene samples and subsequently baked at 180°C for half an hour. Then we carefully pasted a piece of Scotch transparent tape onto PMMA layer and etched the underlying SiO_2 by KOH aqueous solution, followed by thorough rinsing with DI water and careful drying at 50°C in an oven. Then the graphene/PMMA/tape sample was align-transferred onto the prepared BN flake. Finally the samples were carefully cleaned with acetone and isopropyl alcohol (Fig. S1c). AFM of the GBN samples was carried out in a Bruker Multimode 8 microscope under tapping mode.

Raman spectroscopy and mapping of GBN. Raman spectroscopy and mapping was done on a Horiba Jobin-Yvon HR800 confocal Raman microscope with a 633 nm He-Ne laser excitation and a liquid-nitrogen-cooled CCD detector (data from Fig. 2a and 2b in the main text). For each GBN sample, we usually mapped a 3 um × 3 um area with a 0.1 or 0.2 um steps. The mapping data in Fig. 2c and d was done using a 514 nm laser excitation. To avoid excessive heating effect on graphene, 2 mW laser power was used for all Raman measurements. We did AFM before and after Raman mapping to confirm that the bubbles were not damaged by the laser heating during Raman mapping.

1. Geim, A. K. & Novoselov, K. S. The rise of graphene. *Nat. Mater.* **6**, 183–191 (2007).
2. Schwierz, F. Graphene transistors. *Nat. Nanotechnol.* **5**, 487–496 (2010).
3. Castro Neto, A. H., Novoselov, K. S. & Geim, A. K. The electronic properties of graphene. *Rev. Mod. Phys.* **81**, 109–162 (2009).
4. Dean, C. R. *et al.* Boron nitride substrates for high-quality graphene electronics. *Nat. Nanotechnol.* **5**, 722–726 (2010).
5. Dean, C. R. *et al.* Graphene based heterostructures. *Solid Stat. Comm.* **152**, 1275–1282 (2012).
6. Xue, J. *et al.* Scanning tunneling microscopy and spectroscopy of ultra-flat graphene on hexagonal boron nitride. *Nat. Mater.* **10**, 282–285 (2011).
7. Mayorov, A. S. *et al.* Micrometer-scale ballistic transport in encapsulated graphene at room temperature. *Nano Lett.* **11**, 2396–2399 (2011).
8. Gannett, W., Regan, W., Watanabe, K., Taniguchi, T., Crommie, M. F. & Zettl, A. *Appl. Phys. Lett.* **98**, 242105 (2011).
9. Britnell, L. *et al.* Field-effect tunneling transistor based on vertical graphene heterostructures. *Science* **335**, 947–950 (2012).
10. Guinea, F., Katsnelson, M. I. & Geim, A. K. Energy gaps and zero-field quantum Hall effect in graphene by strain engineering. *Nat. Phys.* **6**, 30–33 (2010).
11. Guinea, F., Katsnelson, M. I. & Vozmediano, M. A. H. Midgap states and charge inhomogeneities in corrugated graphene. *Phys. Rev. B* **77**, 075422 (2008).
12. Pereira, V. M. & Castro Neto, A. H. Strain engineering of graphene's electronic structure. *Phys. Rev. Lett.* **103**, 046801 (2009).
13. Low, T., Guinea, F. & Katsnelson, M. I. Gaps tunable by electrostatic gates in strained graphene. *Phys. Rev. B* **83**, 195436 (2011).
14. Guinea, F., Geim, A. K., Katsnelson, M. I. & Novoselov, K. S. Generating quantizing pseudomagnetic fields by bending graphene ribbons. *Phys. Rev. B* **81**, 035408 (2010).
15. Ni, Z. H., Yu, T., Lu, Y. H., Wang, Y. Y., Feng, Y. P. & Shen, Z. X. Uniaxial strain on graphene: spectroscopy study and band-gap opening. *ACS Nano* **2**, 2301–2305 (2008).
16. Levy, N. *et al.* Strain-induced pseudo-magnetic field greater than 300 tesla in graphene nanobubbles. *Science* **329**, 544–547 (2010).
17. Bao, W. *et al.* Controlled ripple texturing of suspended graphene and ultrathin graphite membranes. *Nat. Nanotechnol* **4**, 562–566 (2009).
18. Yoon, D., Son, Y.-W. & Cheong, H. Negative thermal expansion coefficient of graphene measured by Raman spectroscopy. *Nano Lett.* **11**, 3227–3231 (2011).
19. Lu, J., Castro Neto, A. H. & Loh, K. P. Transforming Morie blisters into geometric graphene nano-bubbles. *Nat. Comm.* **3**, 823 (2012).
20. Liu, B., Yu, M.-F. & Huang, Y. Role of lattice registry in the full collapse and twist formation of carbon Nanotubes. *Phys. Rev. B* **70**, 161402(R) (2004).
21. Xiao, J., Liu, B., Huang, Y., Zuo, J., Hwang, K.-C. & Yu, M.-F. Collapse and stability of single- and multi-wall carbon Nanotubes. *Nanotechnology* **18**, 395703 (2007).
22. Ferralis, N. Probing mechanical properties of graphene with Raman spectroscopy. *J. Mater. Sci.* **45**, 5135–5149 (2010).
23. Huang, M., Yan, H., Chen, C., Song, D., Heinz, T. F. & Hone, J. Phonon softening and crystallographic orientation of strained graphene studied by Raman spectroscopy. *PNAS* **106**, 7304–7308 (2009).
24. Tsoukleri, G. Subjecting a graphene monolayer to tension and compression. *Small* **5**, 2397–2402 (2009).
25. Das, A. *et al.* Monitoring dopants by Raman scattering in an electrochemically top-gated graphene transistor. *Nat. Nanotechnol* **3**, 210–215 (2008).
26. Pisana, S. *et al.* Breakdown of the adiabatic Born-Oppenheimer approximation in graphene. *Nat. Mater.* **6**, 198–201 (2007).
27. Mohiuddin, T. M. G. *et al.* Uniaxial strain in graphene by Raman spectroscopy: G peak splitting, Gruneisen parameters, and sample orientation. *Phys. Rev. B* **79**, 205433 (2009).
28. Zabel, J. *et al.* Raman spectroscopy of graphene and bilayer under biaxial strain: bubbles and balloons. *Nano Lett.* **12**, 617–621 (2012).
29. Mounet, N. & Marzari, N. First-principle determination of the structural, vibrational and thermodynamic properties of diamond, graphite, and derivatives. *Phys. Rev. B* **71**, 205214 (2005).
30. Freund, L. B. & Suresh, S. Thin Film Materials: Stress, Defect Formation and Surface Evolution, Cambridge University Press, Cambridge, UK, 2003.
31. Wang, Z. F., Zhang, Y. & Liu, F. Formation of hydrogenated graphene nanoripples by strain engineering and directed surface self-assembly. *Phys. Rev. B* **83**, 041403(R) (2011)
32. Zomer, P. J., Dash, S. P., Tombros, N. & van Wees, B. J. A transfer technique for high mobility graphene devices on commercially available hexagonal boron nitride. *Appl. Phys. Lett.* **99**, 232104 (2011).
33. Zhu, L., Wang, Z., Wang, Y., Zou, G., Mao, H. & Ma, Y. Bending ultrathin graphene at the margins of continuum mechanics. *Phys. Rev. Lett.* **106**, 255503 (2011).
34. Pease, R. S. An X-ray study of boron nitride. *Acta Cryst* **5**, 356 (1952).
35. Bonini, N., Garg, J. & Marzari, N. Acoustic phonon lifetimes and thermal transport in free-standing and strained graphene. *Nano Lett* **12**, 2673–2678 (2012).
36. Georgiou, T. *et al.* Graphene bubbles with controllable curvature. *Appl. Phys. Lett.* **99**, 093103 (2011).
37. Stolyarova, E. *et al.* Observation of graphene bubbles and effective mass transport under graphene films. *Nano Lett* **9**, 332–337 (2009).
38. Tersoff, J. Modeling solid-state chemistry: interatomic potentials for multicomponent systems. *Phys Rev B* **39**, 5566 (1989).

39. Haigh, S. J. *et al.* Graphene-based heterostructures and superlattices: cross-sectional imaging of individual layers and buried interfaces. arXiv:1206.6689v1 (2012).

Author contributions

X. W., Y. S. and W. P. conceived the project. W. P., J. Z. and Z. N. carried out the experiments. J. X. did the finite element mechanical modeling. C. Y. and G. Z. did the molecular dynamics simulations. K. W. and T. T. provided the BN samples. W. P., J. X., Y. S. and X. W. co-wrote the paper. All authors reviewed and commented on the manuscript.

Additional information

Supplementary information accompanies this paper at http://www.nature.com/scientificreports

Competing financial interests The authors declare no competing financial interests.

How to cite this article: Pan, W. *et al.* Biaxial Compressive Strain Engineering in Graphene/Boron Nitride Heterostructures. *Sci. Rep.* **2**, 893; DOI:10.1038/srep00893 (2012).